Physica Medica 63 (2019) 63–69

Contents lists available at ScienceDirect

Physica Medica

journal homepage: www.elsevier.com/locate/ejmp

Original paper

A real-time, single-exposure, dual-energy subtraction mask for markerless tumor tracking in radiotherapy: Proof of concept

Shinichiro Mori

Research Center for Charged Particle Therapy, National Institute of Radiological Sciences, Inage-ku, Chiba 263-8555, Japan

ARTICLE INFO

Keywords:
Radiation therapy
Dual energy subtraction
Fluoroscopy
Gating

ABSTRACT

Introduction: Bone density can interfere with fluoroscopy-guided tumor tracking in radiotherapy. To improve markerless tumor tracking accuracy, we developed a dual energy subtraction (DES) mechanical image mask to use with a single x-ray exposure.

Methods: The DES mask consists of 2-mm-thick stainless-steel with 128 pairs of slits (0.388 mm width and openings), designed to match the dynamic flat panel detector (DFPD) pixel size. This was set on the front of the DFPD. This results in a DFPD image with one containing the exposed pixels and one containing the masked pixels. The masked pixel columns were interpolated from adjacent pixels and a subtraction image was generated from the interpolated images to make a bone suppression (BS) image. A chest phantom was set on the commercially available moving table (CIRS DYNAMIC PLATFORM 008PL) and DFPD images were acquired. A reference BS image was generated by double-exposure DES with and without a 2-mm-thick stainless-steel plate. Image quality and markerless tumor tracking accuracy were then evaluated.

Results: The DES mask decreased most of the visible bone densities from the chest phantom image acquired with a single exposure for a peak-signal-to-noise-ratio/structural similarity index measure (PSNR/SSIM) of 25.3 db/0.685). The tracking positional error, originally 12.6 mm, was improved to 0.2 mm.

Conclusions: The DES mask can aid in BS image on fluoroscopic imaging and may be useful in markerless tumor tracking.

1. Introduction

External surrogate motion monitoring is widely used in thoraco-abdominal radiotherapy [1,2]. Although it is not invasive to the patient and can be easily implemented, this approach assumes that surface respiratory movement correlates closely with internal tumor position. In actual treatment situations, especially in the chest, this correlation does not always apply [3–5]. To solve this problem, fluoroscopy-based respiratory gating approaches have been introduced to capture tumor position during treatment. There are two types of tracking methods, those using surgically placed fiducial markers, and markerless tracking [6–9]. The marker tracking approach was introduced in the 1990s [6] and is now commercially available (CyberKnife Robotic Radiosurgery System, Accuray, Inc.; Sunnyvale CA USA; and SyncTraX, Shimadzu, Kyoto, Japan). More advances have been gained in the markerless technique [8]. Image-guided radiotherapy techniques, including image processing, computer vision, and machine learning, are capable of monitoring tumor position fluoroscopically in real time. Our hospital began using fluoroscopy-based markerless tumor tracking in 2015 for carbon-ion scanning beam treatments, including in the thoraco-abdominal region [10].

One of the problems in markerless tumor tracking in lung cancer, which detects tumor position by using fluoroscopic images in a real-time, in lung cancer is that during administration of a fraction, lung tumors generally move in the opposite direction to the ribs during the respiratory cycle, which could degrade tracking accuracy. One solution to this problem is bone suppression (BS), which provides a clearer image by removing bone densities on the x-ray image (BS image). Dual energy subtraction (DES) imaging may be performed using two different x-ray energies (double-exposure DES) or by sandwiching a thin metal filter between two detectors (single-exposure DES) [11,12]. Double-exposure DES imaging is now commercially available and, along with fast x-ray switching, is the only imaging technique able to acquire real-time DES fluoroscopic images. However, organ positional differences due to respiratory and cardiac motion may degrade quality of the DES image because it cannot obtain two different energy images at the same time, despite fast energy switching high and low x-ray energies [13,14]. The latest commercially available x-ray fluoroscopic imaging system acquires each energy image at 30 frame per second (the delay time of energy switching is approximately 15 frame per second),

E-mail address: shinshin@nirs.go.jp.

https://doi.org/10.1016/j.ejmp.2019.05.015
Received 19 December 2018; Received in revised form 10 May 2019; Accepted 18 May 2019
Available online 29 May 2019

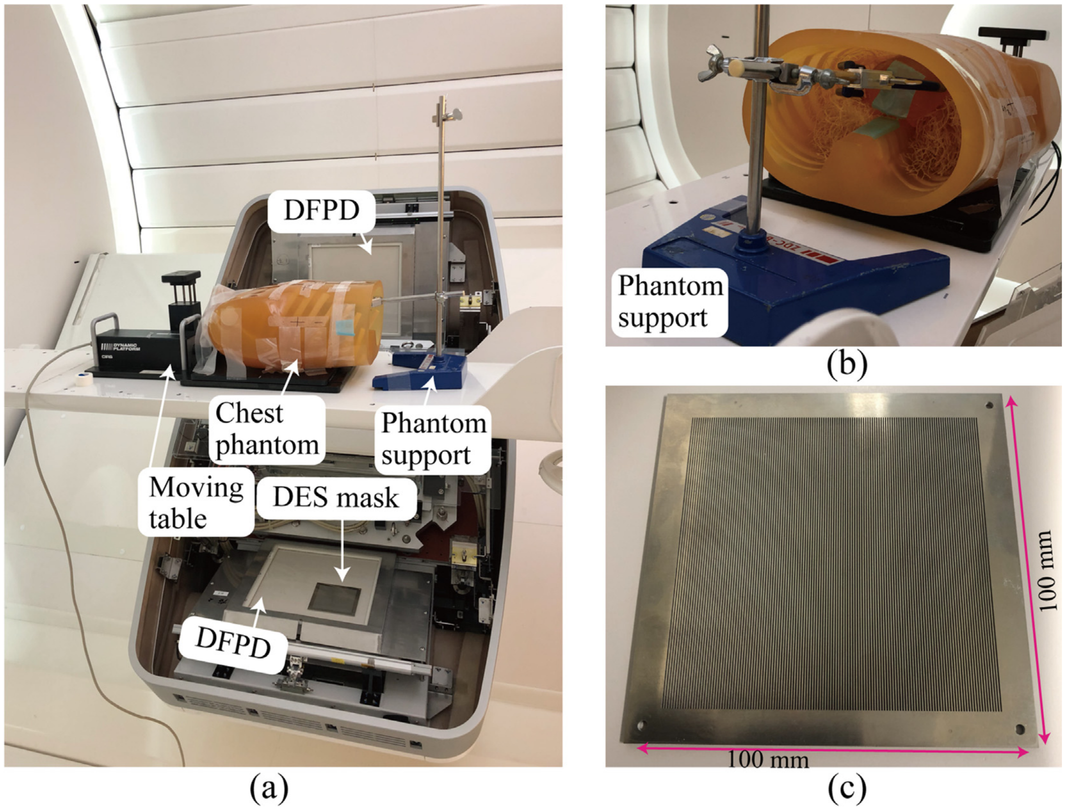

Fig. 1. Experimental setup for the (a) DES mask and chest phantom. Gantry angle was set to 135°. (b) Back view of the chest phantom. The phantom support fixed the internal organs. (c) DES mask. *Abbreviations*: DES = dual energy subtraction, DFPD = dynamic flat panel detector.

resulting in a greatly improved DES image quality. While single-exposure DES imaging generally uses x-ray film or an imaging plate; however, it cannot be used with fluoroscopy.

To obtain BS images using another approach in real time, we developed a new pixel mask (DES mask). We generated single-exposure DES images using the DES mask and a chest phantom, comparing it to double-exposure DES images using a stainless-steel plate.

2. Materials and methods

2.1. Dual energy subtraction mask

The DES mask is a 2-mm-thick sheet of SUS304 stainless steel with 128 pairs of 0.388 mm slits and 0.388 mm openings (accuracy [Mean ± SD], 0.381 ± 0.004 mm and 0.392 ± 0.004 mm, respectively), designed to match the dynamic flat panel detector (DFPD) pixel size (Fig. 1a and 1c). We selected this set-up because it was easy to manufacture. The attenuation coefficient of 2 mm SUS304 stainless steel (=2.90 cm^{-1}) is equivalent to 12 mm of aluminum (=0.46 cm^{-1}). The DES mask was set on the front of the DFPD to overlie the mask slit positions on the DFPD pixel positions. To do this, we adjusted the mask position manually by observing DFPD image to minimize the magnitude of vertical stripes. In this study, it took 2 h to set the mask correctly. To evaluate the basic performance of this mask, we produced a prototype model measuring 100 mm × 100 mm (REPIC Corp., Tokyo, Japan).

2.2. Image processing

Image processing was used to generate a DES image. The DFPD image with the DES mask consisted of masked and unmasked pixels (Fig. 2a). Images consisting of masked pixels (Image 1) and of unmasked pixels (Image 2) were generated (Fig. 2b). As an example of this, masked pixels ([$n-2$]th, nth, [$n+2$]th columns) (Image 1) separated from unmasked pixels ([$n-1$]th, [$n+1$]th columns) (Image 2) are shown in the upper and lower panels in Fig. 2b, respectively. Since pixel positions in the ($n-2$)th and ($n+2$)th columns in Image 1 were masked (colored in white in Fig. 2b) (similarly in Image 2), these pixel column values were calculated by interpolating from the adjacent unmasked pixels (Fig. 2c). There are several pixel interpolation methods; we used linear interpolation to calculate the masked pixel values (e.g. pixel value $Pc = [Pa + Pb]/2$ in Fig. 2c). By doing this, all areas in Image 1 and Image 2 were filled by pixel values with and without masking, respectively.

Image 1 was then subtracted from Image 2 by multiplying by the optimum coefficient to create a BS or a soft-tissue-optimized image (Fig. 2d). The optimum coefficient (C) can be obtained as follows. The entrance (I_0) and exit X-ray intensities (I) can be expressed as:

$$I = I_0 \exp(-(\mu_{bone} t_{bone} + \mu_{tissue} t_{tissue})) \tag{1}$$

where μ_{bone} and μ_{tissue} are the linear attenuation coefficients of the bone and tissue, respectively, and t_{bone} and t_{tissue} are the thickness of the bone and tissue, respectively.

We obtained the line integral of the attenuation coefficients along the x-ray path by dividing both sides of Eq. (1) by I_0.

$$D = -\ln\left(\frac{I}{I_0}\right) = \mu_{bone} t_{bone} + \mu_{tissue} t_{tissue} \tag{2}$$

For the DES mask, the D values for the two images acquired by different x-ray energies are expressed by:

$$D_H = \mu_{bone,H} t_{bone} + \mu_{tissue,H} t_{tissue} \text{ (for Image 1)} \tag{3}$$

$$D_L = \mu_{bone,L} t_{bone} + \mu_{tissue,L} t_{tissue} \text{ (for Image 2)} \tag{4}$$

where μ_H and μ_L are the linear attenuation coefficients for high and low x-ray energies, respectively.

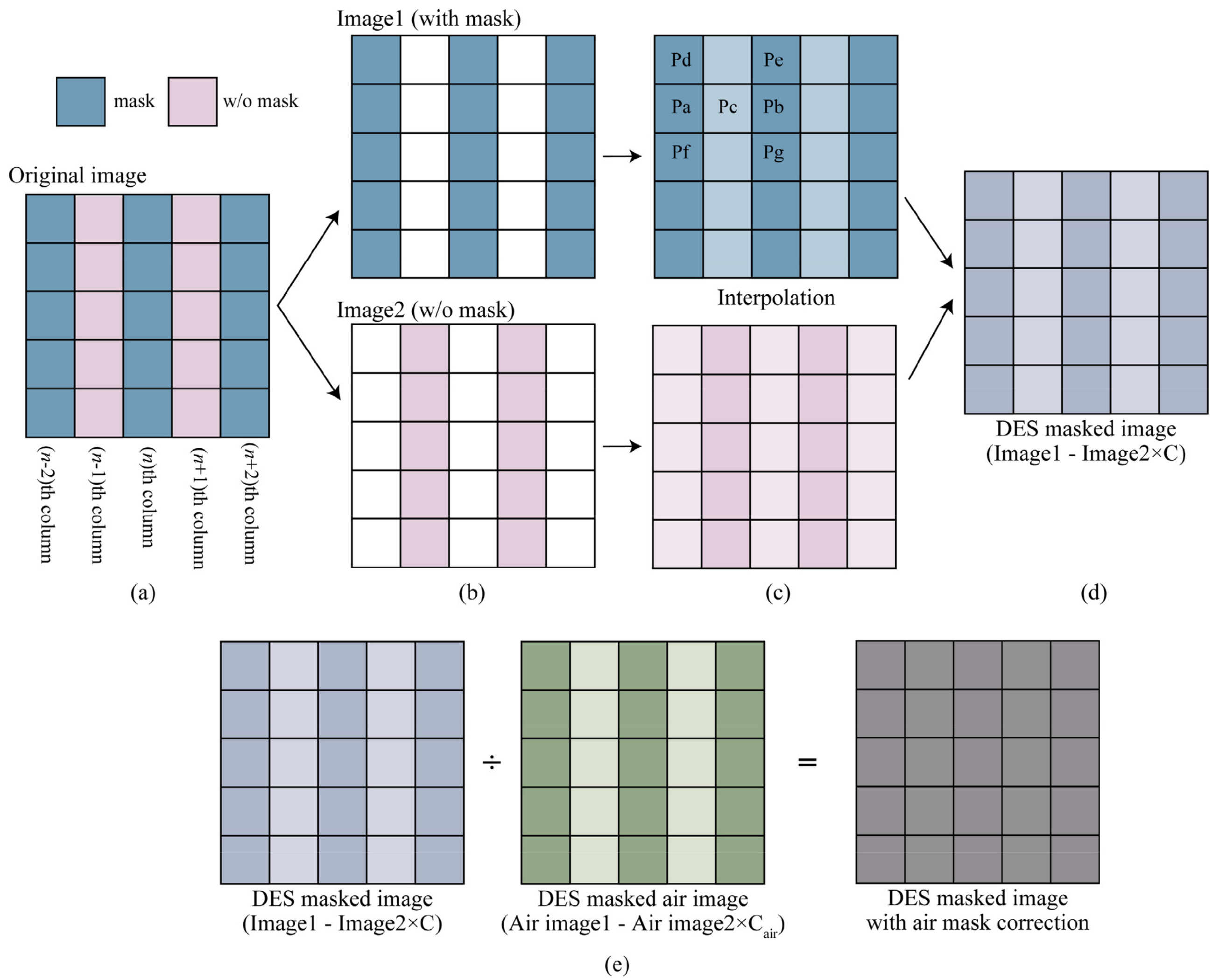

Fig. 2. Image processing for generating a dual energy subtraction (DES) image with the DES mask. (a) Original DFPD image with the DES mask. (b) Separated images with and without masking. (c) Images with interpolated masked pixel values. (d) DES masked image (bone suppression image). (e) DES masked image with air mask correction (bone suppression image).

We obtained the BS image by subtracting D_L multiplied by the coefficient C from D_H as follows:

$$Image_{tissue} = D_H - C\bullet D_L \tag{5}$$

where $C = \frac{\mu_{bone,H}}{\mu_{bone,L}}$.

We have described the above equations assuming monochromatic x-ray flux; where necessary, however, we performed fine adjustment to the coefficient C empirically to emphasize tissue regions due to polychromatic x-ray flux.

However, the DES mask image retained some white and gray vertical bands due to positional/production inaccuracies (Fig. 3b). To correct this, we divided the DES mask image (Fig. 3b) by the DES mask air image (Fig. 3a) (air mask correction). A processed DES image of air would ideally show uniform pixel values; however, the actual image retains a striped pattern (Fig. 3a). By doing this, the magnitude of the vertical bands can be minimized in the final DES image (Fig. 3c). However, vertical bands were still remained in two grids, which were warped due to handling carelessness (marked as red arrows in Fig. 3c). All image processing was programmed in Microsoft Visual Studio 2013 (Microsoft Corp, Redmond WA, USA) and performed on a workstation (Dell Precision 540, 2.0 GHz single quad-core CPU Intel Xeon processor, 4 GB physical memory, Windows 7). X-ray image data (768 × 768 pixels) was sent to the workstation. The computation time was measured 10,000 times excluding the time for reading the image. The mean computation time was < 1 ms per image.

2.3. Imaging system

We used the DFPD imaging system installed in the carbon-ion beam rotating gantry treatment room. This imaging system consists of paired x-ray fluoroscopy units set up for acquisition with respiratory gating (Fig. 1a). The DFPD is an indirect type of detector (PaxScan 3030 +, Varian Medical Systems, Palo Alto, CA) with an imaging area size of 298 × 298 mm, physical pixel size of 388 μm (2 × 2 binning mode using the original pixel size of 194 μm for fluoroscopic mode) and an amorphous silicon receptor. The image matrix size is 768 × 768 pixels. Distance from the isocenter (ISO) and source-image receptor distance (SID) are 2984 mm and 3695 mm, respectively, allowing acquisition of an image size of approximately 240 × 240 mm at the isocenter. An anti-scatter grid is not used. A pair of DFPDs are installed on the right and left sides of the irradiation port at 45° and 315°, respectively. Gantry angle was 135° to set the DES mask easily.

2.4. Moving phantom

To generate double-exposure DFPD images with the DES mask, we set the chest phantom on the moving table (CIRS DYNAMIC PLATFORM 008PL, Norfolk VA, USA) and the DES mask in front of the DFPD

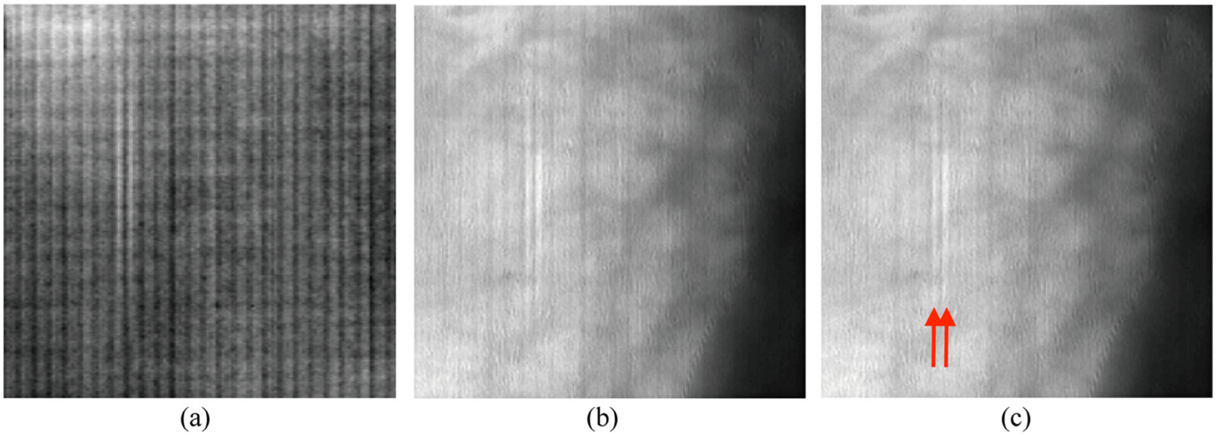

Fig. 3. (a) DES masked air image. (b) DES image without air correction. (c) DES image with air correction. Warped grids due to handling carelessness were marked as red arrows.

(Fig. 1a and 1b). The chest phantom (thoracic phantom; Kyoto Kagaku, Kyoto, Japan) was positioned at the isocenter in the lateral and craniocaudal directions. The chest phantom consisted of two parts: internal organs (heart and lung pulmonary vessels) and chest wall/rib. If both internal and outer parts were moved by the moving table, markerless tumor tracking accuracy might not be changed with and without the DES mask. To simulate patient respiration, the internal organ parts were fixed by the phantom support and the outer part representing the chest wall was moved ± 10 mm sinusoidally in the superior-inferior direction over a 4.0 s respiratory cycle by the moving table (Fig. 1b)

2.5. Evaluation methods

We evaluated DES image quality and markerless tumor tracking accuracy.

To compare the quality of BS images with the DES mask to the reference BS image, we acquired DFPD images with and without a 2 mm SUS304 stainless-steel plate without slits (double-exposure DES imaging), which was set in front of the DFPD. We selected pixel columns alternatively from DFPD images with and without the stainless-steel plate. Image processing was performed as described in the previous section to obtain a BS image. The quality of the BS image with the DES mask was compared to that of the reference BS image using the visual observation by medical physicist who has over 15 years clinical experiences and the peak signal-to-noise ratio (PSNR), structural similarity index measure (SSIM), and signal-to-noise ratio (SNR) [15]. Both metrics are widely used to measure the similarity between two images quantitatively, with high PSNR and SSIM values indicating high similarity. It is difficult for PSNR to distinguish between a large pixel value difference in a single pixel and small pixel value differences in several pixels. Furthermore, PSNR is more sensitive to simple object structures than complex object structures, even those with large pixel value differences. Because PSNR and human visual perception can be inconsistent, we used additional metrics, namely SSIM, which measures three metrics (luminance, contrast, and structure) in small respective windows. This solved the limitations of PSNR. The SSIM value was shown to reflect human visual perception well.

$$PSNR = 10\bullet\log_{10}\frac{MAX^2}{MSE}, \tag{6}$$

where MAX is the maximum pixel value of the input image, and MSE is the mean square error.

$$MSE = \frac{1}{mn}\sum_{x=0}^{m-1}\sum_{y=0}^{n-1}[IM_{ref}(x, y) - IM_{mask}(x, y)]^2, \tag{7}$$

where m and n are the number of image matrices, IM_{ref} and IM_{mask} are the reference and DES mask BS images, respectively.

$$SSIM = \frac{(2\psi_{ref}\psi_{mask} + c_1)(2\sigma_{ref,mask} + c_2)}{(\psi_{ref}^2 + \psi_{mask}^2 + c_1)(\sigma_{ref}^2 + \sigma_{mask}^2 + c_2)}, \tag{8}$$

where ψ_{ref}, ψ_{mask}, σ_{ref}, and σ_{mask} are the mean pixel values of the reference BS image, the DES mask BS image, the standard deviation (SD) of the reference BS image, and the SD of the DES mask BS image, respectively. $\sigma_{ref,mask}$ is the covariance of the reference BS and DES mask BS images.

The quality of the DES mask BS image was compared with that of the original image as well as with that of the reference BS image.

$$SNR = 20\bullet\log_{10}\left(\frac{MAX - MIN}{\sigma}\right), \tag{9}$$

where MIN and σ are minimum pixel values and the SD of the input image.

The chest phantom was not moved for this evaluation. Image acquisition conditions were tube currents of 100 mA, and exposure time per frame of 40 ms. A tube voltage of 100 kVp was selected from our routine imaging conditions. We obtained 20 images and averaged them to improve image noise (recursive filter) and applied the DES mask image processing to assess bone suppression.

For markerless tumor tracking, we used single- and multi-template image matching to emphasize tumor tracking accuracy differences using the image with and without the DES mask. Template size was 150 × 150 pixels and set on the center of the image position at peak exhalation. The similarity index was the mean square error. For the multi-template matching algorithm, a total of 10 template images were selected from the fluoroscopic images for a single respiratory cycle [8].

The chest phantom was moved. Since the chest wall/rib structures were moved sinusoidally, but internal organs were not moved, the markerless tumor tracking would result in the same position as a function of time. Image acquisition conditions were the same as those in the image quality study and the respiratory cycle was 4 s, but the imaging time was set at approximately 2 s to include the whole phantom displacement and applied the recursive filter to 5 consecutive frames.

All evaluations were performed using a commercial programming environment (MATLAB R2018a©, Mathworks, Natick MA, USA).

3. Results

3.1. Image quality

We acquired DFPD images of the chest phantom with and without the DES mask at three different locations (left upper lobe, left lower

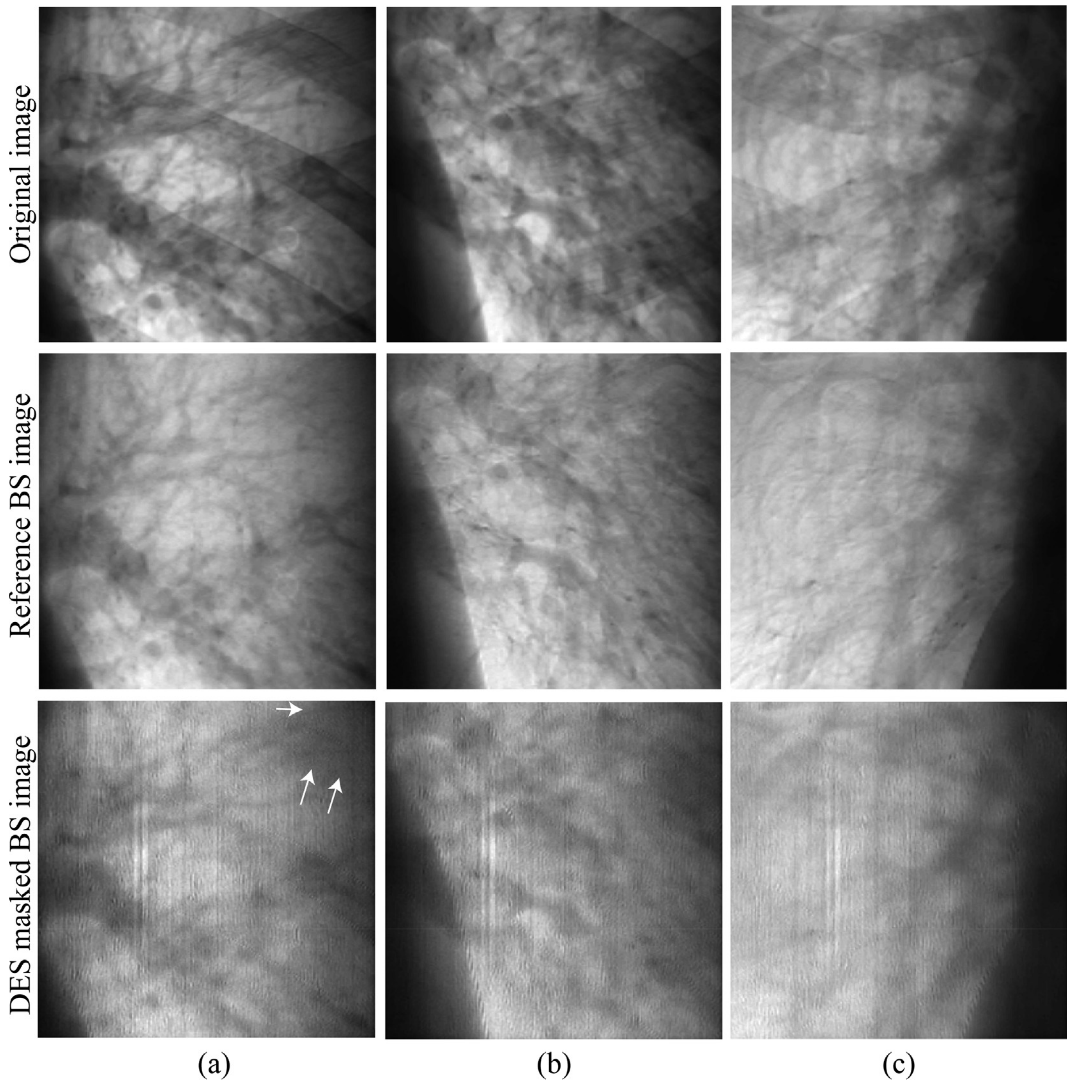

Fig. 4. Chest phantom dynamic flat panel detector (DFPD) images of (a) left upper lobe, (b) left lower lung, and (c) right middle lobe. The upper panel shows the original DFPD images without the dual energy subtraction (DES) mask. The middle panel shows the reference bone suppression (BS) images with and without the stainless-steel plate. The lower panel shows the BS images with the DES mask.

lung, and right middle lung lobe) (Fig. 4). Bone and soft tissues were clearly visible in the original DFPD image (upper panel in Fig. 4). The image obtained by double exposure imaging with the stainless-steel plate (reference BS images) successfully removed bone structures (middle panel in Fig. 4). The BS images with the DES mask substantially suppressed them compared to the original DFPD images (lower panel in Fig. 4), but the mask did not completely remove high-contrast bone structures (marked as arrows in Fig. 4a). Minute structures were not clearly observed by comparing with those in the reference BS images. DES images still displayed pixel value variation in the form of vertical stripes.

Quantitative analysis is summarized in Table 1. PSNR and SSIM values of the DES mask image averaged over the three lung regions were 24.2 db and 0.675, respectively. By applying the air mask correction, the quality of the DES mask image was improved to 25.3 db/0.685 (PSNR/SSIM).

SNR values averaged over the three lung regions were 17.1 dB and 13.3 dB for the images with and without mask, respectively (Table 2).

3.2. Tracking accuracy

Markerless tracking positional error was expressed in Euclidian

Table 1
Results of image quality assessment for PSNR and SSIM.

Image type	Air mask correction	Left upper lung lobe		Left middle lung lobe		Right middle lung lobe		Mean	
		PSNR [db]	SSIM	PSNR [db]	SSIM	PSNR [db]	SSIM	PSNR [db]	SSIM
DES mask BS image – Reference BS image	No	24.0	0.637	23.3	0.680	25.3	0.708	24.2	0.675
	Yes	24.9	0.650	24.6	0.685	26.5	0.719	25.3	0.685
DES mask BS image – Original image	No	20.9	0.538	21.2	0.601	23.0	0.655	21.7	0.598
	Yes	22.1	0.545	21.1	0.593	22.7	0.651	22.0	0.596

Abbreviations: DES = dual energy subtraction, PSNR = peak signal-to-noise ratio, SSIM = structural similarity index measure.

Table 2
Results of image quality assessment for SNR.

Image type	Left upper lobe	Left midlung	Right middle lobe	units: dB Mean
With mask	15.1	13.0	23.2	17.1
Without mask	13.0	11.2	15.5	13.3

Abbreviations: SNR = signal to noise ratio.

distance by calculating positions for respective image frames minus that for the first image frame (Fig. 5 and Table 3). For the single template matching algorithm, markerless tracking using the original image was inaccurate due to high contrast bone structures, with a tracking error of 12.57 mm ± 16.43 mm (< 41.85 mm). The tracking error using the reference BS images showed much better accuracy (< 0.1 mm). The BS image with the DES mask improved the tracking error close to those of the reference BS image (< 0.27 mm).

With the multi-template matching algorithm, the tracking error using the original image was much improved over that using the simple-template matching algorithm using the original image (=0.30 mm ± 0.10 mm [< 0.63 mm]). Moreover, the tracking error using the reference BS image and BS image with DES mask was < 0.1 mm.

4. Discussion

We developed a prototype DES mask and generated BS images of a chest phantom in double-exposure and single-exposure studies. Compared to the reference BS image in double-exposure, the magnitude of BS was moderately smaller in the single-exposure study; however, the DES mask proved capable of providing BS on fluoroscopic images in real time.

The image processing involved takes less than 1 ms per image. Another approach to BS, machine learning [16], is now commercially available (Clear Read Bone Suppression; Riverain Technologies, Miamisburg OH, USA). Tracking accuracy was improved using BS [17]; however, this machine leaning approach took several seconds per image, rendering it impossible to apply to real-time imaging.

Since the BS image with the DES mask is obtained during a single exposure, object positional variation during imaging is not an issue. This improves image quality around the heart and mediastinum. Although cardiac gating for DES imaging has been proposed [14], use of the DES mask is more convenient.

For markerless tracking, even though the underlying organs in the phantom did not move as an actual patient, our study showed the BS image improved markerless tracking accuracy; however, this improvement was dependent on the tracking algorithm. Since patient anatomical structures were moved deformably due to intrafractional

Table 3
Tracking error results using the single- and multi-template matching algorithms.

Tracking algorithm	Image type	Tracking error (mm)			
		Mean	±	SD	Maximum
Single template matching	Original image	12.57	±	16.43	41.85
	Reference BS image	0.03	±	0.03	0.10
	BS image with DES mask	0.16	±	0.10	0.27
Multi-template matching	Original image	0.30	±	0.10	0.63
	Reference BS image	0.02	±	0.02	0.08
	BS image with DES mask	0.01	±	0.01	0.03

Abbreviations: DES = dual energy subtraction, SD = standard deviation.

respiratory motion, it is difficult to capture tumor position using a single template image, which is not generally used in clinical situations. To solve this problem, several researchers introduced markerless tracking algorithms such as the multi-template matching and machine learning approaches [8,18–20]. Patel et al. evaluated markerless lung tumor tracking accuracy and found that tracking accuracy was slightly improved by using BS images (1.4 ± 1.1 mm from 2.0 ± 1.3 mm) [21]. This is because they calculated similarity scores using different image modalities (CT-based template and fluoroscopic images), which could result in degradation of the similarity score. A few studies introduced markerless tumor tracking using patient lung fluoroscopic BS images [22,23]. Tanaka et al. evaluated tracking accuracy using patient lung fluoroscopic BS images with fluoroscopic image-based template matching [22]. They concluded that tracking error was improved to 3.0 ± 1.1 mm for the dual-energy image from 28.1 ± 20.0 mm for the single-energy image, similar to our results.

With regard to the imaging dose, the DES mask was expected to result in a lower dose than that with double-exposure DES imaging, because the DES mask resulted in high and low x-ray energy doses to half area in a single image to calculate the BS image. However, use of a 2-mm-thick stainless-steel plate reduced the imaging dose by 80%. We did not evaluate optimum mAs values, however, for double-exposure imaging with a stainless-steel plate. A 5× higher dose with the slit mask is required to obtain the same dose without the slit mask by the changing mAs value for each image acquisition. As a result, the total imaging dose was 2× higher than that of conventional imaging 1.0[*withoutslitmask*] + 0.2[*withslit*] × 5 (10) Since the DES mask imaging used a single exposure, mAs values should be adjusted to obtain sufficient image quality with the slit mask. The imaging dose without the slit mask could be excessive. To obtain the same image quality with the slit mask, the total imaging dose was 3 times (=(1.0 [without slit mask] + 0.2 [with slit mask])/2 [half area for each] × 5) higher than

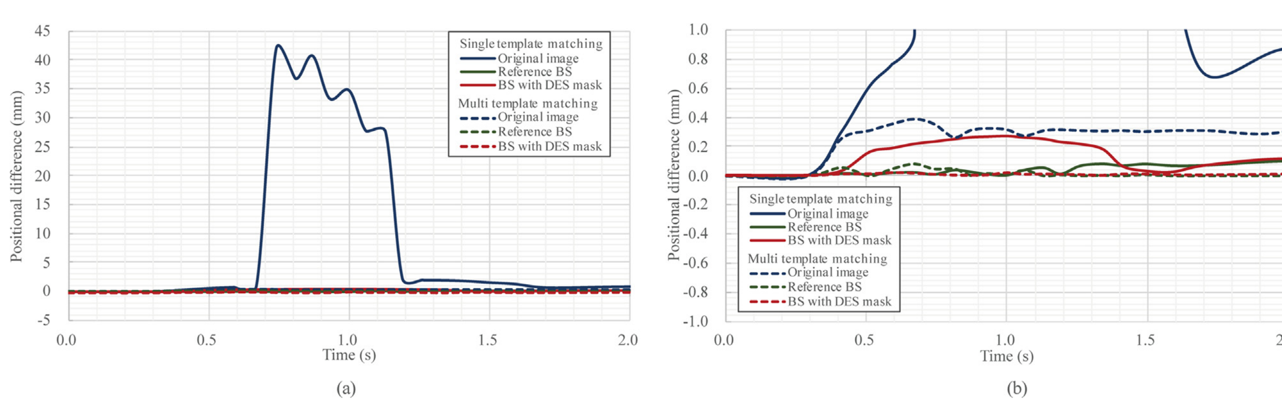

Fig. 5. Markerless tumor tracking positional differences (expressed in Euclidian distance) for the original image, the reference bone suppression (BS) images and the BS images with the DES mask. The tracking algorithms used were single-template and multi-template matching. (a) Full scale view. (b) Enlarged scale view.

that of conventional imaging. This is a simple dose estimation, but the DES mask imaging was able to increase the imaging dose to obtain BS images.

In this study, however, we acquired the original images, the reference BS images, and the DES-masked BS images under the same fluoroscopic image conditions; therefore, the imaging dose was expected to be 1.2 times (= 1.0 [without slit mask] + 0.2 [with slit mask]) higher than that of conventional imaging for the double-exposure imaging and 0.6 times (= (1.0 [without slit mask] + 0.2 [with slit mask])/2 [half area for each]) higher than that of conventional imaging for the DES masked image. Under the fluoroscopic imaging conditions in this study, the pixel values without and with slit mask were not saturated and starved, respectively (Fig. 5).

From our clinical experience with markerless tumor tracking, the x-ray imaging time for a lung case was 1.1–4.4 min per beam; therefore, the imaging dose per beam was 3.3–13.2 mGy [10]. Since we increased the imaging dose to reduce image noise in this study (40 mA, 4 ms/frame to 100 mA, 40 ms/frame), the imaging dose with the DES mask was estimated to be 82.5–329.9 mGy. This is because, as described below, the prototype DES mask installation positional error strongly affected the image quality. More exact installation positions could reduce imaging dose.

Installation cost is an important factor. Single-exposure with fast x-ray switching requires a special x-ray control system. Recently, multiple-layer detectors have been integrated into a commercial CT (IQon Spectral CT, Philips Co., Eindhoven, the Netherlands), allowing it to obtain two different x-ray energy images simultaneously. This degree of detection comes at a large financial cost, but it is one-time capital cost. Using a mask attached to the DFPD, the cost is expected to be much lower than that of the above systems.

A few limitations of this study should be discussed. First, this mask was just a prototype, and should it enter production, methods would be implemented to achieve a more exact installation position. The DES mask ideally shades one pixel while the adjacent pixel is completely unfiltered by the slit to make the BS image; the mask production accuracy and installation positional accuracy could therefore affect the image quality. While the DFPD imaging system was used for both patient setup verification and tumor tracking, it would be possible to use DFPD images with interpolated masked or unmasked pixel values; however, the DES mask would not be mounted permanently, but rather placed on the panel for the tracking process, on the basis that patient setup verification requires images with high spatial resolution.

Second, since the DES mask thickness was 2 mm, scattered radiation could affect adjacent pixel values. A thinner lead mask (approximately 0.1 mm thickness) may address this issue.

Third, we derived the coefficient C by using equation (5), however, it is not a monochromatic x-ray flux we used. We, therefore, performed fine adjustment it manually by visual observation. However, it is necessary to develop the method to define the optimum C value in clinical situations. We would like to develop it in the next study.

Fourth, we did not evaluate the quality of patient image but only that of the phantom image, because the DES mask has not yet obtained pharmaceutical approval (Pharmaceutical Affairs regulatory in Japan). After getting it, we would like to evaluate the quality of patient image with the DES mask.

5. Conclusion

The DES mask minimized most of the visible bone densities from the chest phantom in a single exposure. However, the prototype of the DES mask image still retained some vertical band-like artifacts due to positional/production inaccuracies, necessitating a solution to these problems to improve image quality. Imaging dose with the DES mask was expected to be lower than that with double-exposure DES imaging; however, the prototype of the DES mask required higher doses due to the reason stated above. Moreover, markerless tumor tracking accuracy is dependent on the tracking algorithm, although use of the DES mask did not adversely impact tracking.

References

[1] Bengua G, Ishikawa M, Sutherland K, Horita K, Yamazaki R, Fujita K, et al. Evaluation of the effectiveness of the stereotactic body frame in reducing respiratory intrafractional organ motion using the real-time tumor-tracking radiotherapy system. Int J Radiat Oncol Biol Phys 2010;77:630–6.
[2] Dong B, Graves YJ, Jia X, Jiang SB. Optimal surface marker locations for tumor motion estimation in lung cancer radiotherapy. Phys Med Biol 2012;57:8201–15.
[3] Beddar AS, Kainz K, Briere TM, Tsunashima Y, Pan TS, Prado K, et al. Correlation between internal fiducial tumor motion and external marker motion for liver tumors imaged with 4D-CT. Int J Radiat Oncol. 2007;67:630–8.
[4] Ozhasoglu C, Murphy MJ. Issues in respiratory motion compensation during external-beam radiotherapy. Int J Radiat Oncol. 2002;52:1389–99.
[5] Gierga DP, Brewer J, Sharp GC, Betke M, Willett CG, Chen GTY. The correlation between internal and external markers for abdominal tumors: implications for respiratory gating (vol 61, pg 1551, 2005). Int J Radiat Oncol 2005;62:1257.
[6] Shirato H, Shimizu S, Shimizu T, Nishioka T, Miyasaka K. Real-time tumour-tracking radiotherapy. Lancet (London, England) 1999;353:1331–2.
[7] Nuyttens JJ, Prevost JB, Praag J, Hoogeman M, Van Klaveren RJ, Levendag PC, et al. Lung tumor tracking during stereotactic radiotherapy treatment with the CyberKnife: marker placement and early results. Acta Oncol 2006;45:961–5.
[8] Cui Y, Dy JG, Sharp GC, Alexander B, Jiang SB. Multiple template-based fluoroscopic tracking of lung tumor mass without implanted fiducial markers. Phys Med Biol 2007;52:6229–42.
[9] Lin T, Cervino LI, Tang X, Vasconcelos N, Jiang SB. Fluoroscopic tumor tracking for image-guided lung cancer radiotherapy. Phys Med Biol 2009;54:981–92.
[10] Mori S, Karube M, Shirai T, Tajiri M, Takekoshi T, Miki K, et al. Carbon-ion pencil beam scanning treatment with gated markerless tumor tracking: an analysis of positional accuracy. Int J Radiat Oncol Biol Phys 2016;95:258–66.
[11] Chakraborty DP, Barnes GT. An energy sensitive cassette for dual-energy mammography. Med Phys 1989;16:7–13.
[12] Molloi SY, Mistretta CA. Quantification techniques for dual-energy cardiac imaging. Med Phys 1989;16:209–17.
[13] Alvarez RE, Seibert JA, Thompson SK. Comparison of dual energy detector system performance. Med Phys 2004;31:556–65.
[14] Shkumat NA, Siewerdsen JH, Dhanantwari AC, Williams DB, Paul NS, Yorkston J, et al. Cardiac gating with a pulse oximeter for dual-energy imaging. Phys Med Biol 2008;53:6097–112.
[15] Wang Z, Bovik AC, Sheikh HR, Simoncelli EP. Image quality assessment: from error visibility to structural similarity. IEEE Trans Image Process 2004;13:600–12.
[16] Suzuki K, Abe H, MacMahon H, Doi K. Image-processing technique for suppressing ribs in chest radiographs by means of massive training artificial neural network (MTANN). IEEE Trans Med Imaging 2006;25:406-16.
[17] Xu T, Ducote JL, Wong JT, Molloi S. Dynamic dual-energy chest radiography: a potential tool for lung tissue motion monitoring and kinetic study. Phys Med Biol 2011;56:1191–205.
[18] Zhang X, Homma N, Ichiji K, Takai Y, Yoshizawa M. Tracking tumor boundary in MV-EPID images without implanted markers: a feasibility study. Med Phys 2015;42:2510–23.
[19] Li R, Lewis JH, Cervino LI, Jiang SB. A feasibility study of markerless fluoroscopic gating for lung cancer radiotherapy using 4DCT templates. Phys Med Biol 2009;54:N489–500.
[20] Rostampour N, Jabbari K, Esmaeili M, Mohammadi M, Nabavi S. Markerless respiratory tumor motion prediction using an adaptive neuro-fuzzy approach. J Med Signals Sens 2018;8:25–30.
[21] Patel R, Panfil J, Campana M, Block AM, Harkenrider MM, Surucu M, et al. Markerless motion tracking of lung tumors using dual-energy fluoroscopy. Med Phys 2015;42:254–62.
[22] Tanaka R, Sanada S, Matsui T, Hayashi N, Matsui O. Sequential dual-energy subtraction technique with a dynamic flat-panel detector (FPD): primary study for image-guided radiation therapy (IGRT). Radiol Phys Technol 2008;1:144–50.
[23] Dhont J, Verellen D, Poels K, Tournel K, Burghelea M, Gevaert T, et al. Feasibility of markerless tumor tracking by sequential dual-energy fluoroscopy on a clinical tumor tracking system. Radiother Oncol 2015;117:487–90.